Amphiphile Conformation Impacts Aggregate Morphology and Solution Structure Across Multiple Lengthscales

Michael J. Servis,[a*,†] Biswajit Sadhu,[b*,†,‡] L. Soderholm,[¶] and Aurora E. Clark[*,†,§,‖]

†*Department of Chemistry, Washington State University, Pullman, WA 99164*

‡*Health Physics Division, Bhabha Atomic Research Centre, Mumbai, India*

¶*Chemical Sciences and Engineering Division, Argonne National Laboratory, Argonne, IL 60439*

§*Voiland School of Chemical Engineering and Bioengineering, Washington State University, Pullman, WA 99164*

‖*Pacific Northwest National Laboratory, Richland, WA 99354*

E-mail: mservis@anl.gov; biswajit.sadhu@wsu.edu; auclark@wsu.edu

[a]Current address: Chemical Sciences and Engineering Division, Argonne National Laboratory, Argonne, IL 60439; co-first author

[b]co-first author

Abstract

Although the self-assembly of amphiphiles is well-studied in aqueous solutions, much less is understood about the fundamental driving forces and structure property relationships in non-polar media. In recent work [Journal of Physical Chemistry B, 2020, 124, 10822.] the authors have studied a series of malonomide-based amphiphiles that are relevant to liquid-liquid extraction. That work demonstrated that aggregation is largely driven by local dipole-dipole interactions between molecules. Here, we build upon this observation to develop a more detailed understanding of how the balance of dipole-dipole interactions (controlled by conformation) and molecular architecture influences the morphology of the aggregates across lengthscale. Using constrained molecular dynamics about key degrees of freedom, we demonstrate that the conformation of N,N-dimethyl,N,N-dioctylhexylethoxy malonamide (DMDOHEMA) and N,N-dimethyl,N,N-dibutyltetradecyl malonamide (DMDBTDMA) has a significant impact upon self-association - where appropriate conformational sampling is essential. To quantify the aggregate morphology, several graph theoretic and persistent homology based properties are determined. The former examines the patterns of intermolecular interactions within clusters, while the latter examines the 3-dimensional spatial distribution across lengthscales. Based upon these analyses, we find that the morphology of aggregates, particularly at higher malonamide concentration, depends on a balance of dipole alignment and alkyl tail sterics. Dipole alignment encourages linear patterns of the intermolecular interactions within aggregates, while the the alkyl tail steric interactions between the malonamide result in noticeably less linear aggregates for DMDOHEMA than DMDBTDMA. This is reflected in the spatial distribution, where more holes or voids exist between extractants within the DMDOHEMA that distribute within the solution in more of a "swiss cheese" arrangement as opposed to the more filamentous distribution of DMBDTDMA. This study links conformation and molecular structure to the morphology of amphiphile assemblies, and serves as a basis for ongoing study of multicomponent amphiphile solutions with polar and other solutes, and how these impact aggregation phenomena.

1 Introduction

Supramolecular assembly of amphiphilic molecules supports a breadth of soft matter applications[1] - from catalysis[2] to drug delivery[3] to nano-devices.[4] Aqueous assembly has been the subject of significant study, where many of the fundamental driving forces and structure property relationships have been identified.[5,6] In comparison, organic phase amphiphile assembly is less understood, despite important consequences to several technologies - including liquid-liquid extraction. Liquid-liquid extraction (LLE) is an industrial and analytical process for the selective partitioning of solutes between immiscible liquid phases.[7] Solutes are distributed between low and high dielectric phases by their relative solubilities. This free energy-driven process is controlled, therefore, by solute speciation: for example, target aqueous solutes complex with amphiphilic "extractant" molecules to solubilize the resulting complexes in the low dielectric organic phase. The free energy differences which drive effective separations are often small, including on the order of thermal energy. As a result, relatively minor free energy contributions are essential to understand and model LLE. Among these small free energy contributions is the organic phase aggregation of the extractant and extracted solutes, which imparts mesoscale structure to that phase.[8]

Organic phase aggregation is driven by intermolecular interactions across different energy and length scales. The nanoscopic lengths over which the organization is manifested evades characterization by many experimental techniques: it is too large to probe with techniques including extended X-ray adsorption fine structure (EXAFS), IR or Raman spectroscopy which are sensitive only to local environments while also being too small to effectively interpret using NMR diffusion[9] or small angle scattering data[10–19] fitted with colloidal models. For this reason, a common approach to understanding organic phase aggregation is to combine molecular dynamics (MD) simulation with experimental techniques including small angle X-ray scattering (SAXS).[18,20,21] This provides the benefit of validating the simulation organic phase structure with the experimental data while not relying on ill-suited colloidal models to interpret that data.[22] Instead, validated simulation structure can then be investigated in

detail to bridge atomic and mesoscopic length scales.

In this study, we consider two malonamide extractants commonly applied to f-element separations:[23] N,N'-dimethyl,N,N'-dioctylhexylethoxy malonamide (DMDOHEMA) and N,N'-dimethyl,N,N'-dibutyltetradecyl malonamide (DMDBTDMA), illustrated in Figure 1. To isolate the contributions to organic phase organization from the differences in molecular structure between DMDOHEMA and DMDBTDMA, we consider a simple organic phase: the extractant/solvent mixture in the absence of extracted polar solutes. This system will also serve a baseline from which the impact of extracted solutes can be understood. First, we investigate the impact of extractant conformation and alkyl tail molecular structure on extractant self-association. Then, we apply a graph theoretic and persistent homology approach to quantify both the malonamide aggregate morphology and their associated conformations. The former method provides a detailed understanding of the patterns of intermolecular interactions within and between aggregates, and has been used with much success to characterize complex solutions. The latter provides new and additional insight into the resultant spatial arrangement across lengthscales and represents a powerful emerging tool to connect intermolecular forces and geometric structure. In combination these analytical tools clearly demonstrate that two predominant forces impact aggregate structure for malonomide systems - namely dipole alignment and alkyl tail sterics. Modulation of either of these features influence the interconnectdness of intermolecular interactions within aggregates, inter-aggregate interactions and the resulting geometric arrangement at local and extended lengthscales. This study provides insight into the fundamental drivers of organic phase aggregation and serves as a framework to interpret the effects of chemical structure and composition upon self-assembly and solution organization across lengthscales.

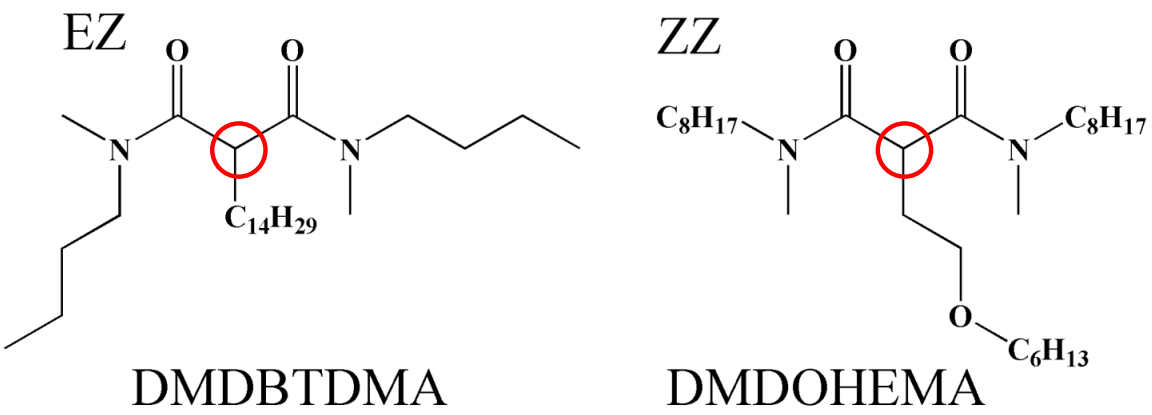

Figure 1: Molecular structures of the two malonamides considered in this study, with the central carbon, "CC," atoms highlighted with red circles. For DMDBTDMA, the two possible amide group conformational isomers are illustrated: E corresponds to the methyl group in the *gauche* configuration while Z refers to the methyl group in the *trans* configuration. For DMDOHEMA, the molecule is drawn with both amide groups in the Z configuration.

2 Simulation and Analysis Methodology

2.1 Molecular Dynamics Simulations

Molecular dynamics simulations employed the GROMACS 2016.2 software package.[24] We previously reported the GAFF-based[25] simulation potentials that are used in this study.[26] Compositions for each system are given in Table 1. Packmol was used to generate random initial configurations for the periodic cell, followed by energy minimization using a steepest descent algorithm. Equations of motion were propagated with a leap-frog Verlet integrator[27] with a 2 fs time step. Hydrogen-containing bonds were constrained with the LINCS algorithm.[28] A 15 Å cutoff was applied for Lennard-Jones interactions and short range electrostatics, with Particle-Mesh Ewald summation used for long-range electrostatics.[29] Systems were equilibrated in the NPT ensemble for 5 ns with a temperature set to 300 K using the velocity rescale thermostat[30] having a 0.2 ps coupling time and pressure set to 1 bar using the Berendsen barostat[30] with a 2 ps coupling time. This was followed by 20, 50 or 100 ns (for 0.5 M, 1.1 M and 1.5 M malonamide systems, respectively) of NVT equilibration with

temperature set to 300 K using the Nosé-Hoover thermostat[31] and a 0.2 ps coupling time. Finally, a 50 ns NVT production trajectory was generated and sampled at 100 ps intervals. The equilibration of the conformational sampling was established through analysis of the time-dependent fluctuations on clustering and spatial distributions as described below and demonstrated in the Supplementary Information (*vide infra*).

Table 1: Molecular compositions and periodic cubic box sizes for the MD simulations. Simulation box dimensions are given in nm and concentrations in mol/L.

DMDOHEMA		DMDBTDMA		Solvent		Simulation box
conc.	num.	conc.	num.	molecule	num.	length (nm)
0.5	301	—	—	n-dodecane	1941	9.890
1.1	662	—	—	n-dodecane	1088	9.911
1.5	903	—	—	n-dodecane	518	9.921
—	—	0.5	301	n-dodecane	2005	9.890
—	—	1.1	662	n-dodecane	1230	9.934
—	—	1.5	903	n-dodecane	713	9.957

2.2 Topological Analyses

Graph Theory Analysis of Intermolecular Interactions. Non-covalent, or supramolecular, self-assembly is driven by local intermolecular interactions that may be represented in a network or graph formalism. This approach is a valuable tool to quantify and characterize the underlying patterns of interactions that govern the morphology of the self-assembled species. Each individual malonamide molecule represents a single node. Edges are drawn between nodes if the positions of the carbon atom bridging the amide groups—referred to here as CC, highlighted in Figure 1—of those two malonamide molecules are within 1.0 nm. The choice of distance cutoff is taken from the CC-CC radial distribution functions (RDF), *vide infra*. The cutoff is consistent between concentrations and the two malonamide molecules.

Once the unweighted, undirected graph defining the malonamide connectivity is constructed, clusters are determined. Clusters are defined as disconnected subgraphs of the

total graph in which all nodes are connected to all other nodes through some path, but are not connected through any path to any other node in a different subgraph. The cluster size is the number of nodes within each subgraph. Within the clusters, several topological properties of their intermolecular interactions are reported as a function of cluster size: global clustering coefficient, average shortest path and maximum shortest path.[32] The global clustering coefficient is defined as the fraction of all triplets within a cluster which are closed, i.e., all three nodes in the triplet are connected to each other. The shortest path between a pair of unique ($i \neq j$) nodes i and j, $d(i,j)$, sometimes referred to as the geodesic, is defined as the length of the path on the graph with the fewest number of edges which connects i and j. The shortest path is computed for all pairs of nodes within each cluster C_n of size n and the average shortest path, a, is defined as

$$a = \frac{1}{n(n-1)} \sum_{i,j \in C_n} d(i,j). \tag{1}$$

Similarly, the maximum shortest path for a given cluster C_n of size n is defined as

$$m = \max_{i,j \in C_n} d(i,j). \tag{2}$$

Topology of Spatial Organization. Complementing the topological characteristics of intermolecular interactions that comprise the amphiphile aggregates, the shape of the aggregates as well as the longer-range spatial organization has been examined. A traditional shape metric, is the radius of gyration, $\mathrm{R_g}$, that is defined as the average root mean squared distance (r_i) of each CC position of node i and the center-of-mass position of all CC atoms in the identified C_n cluster.

$$\mathrm{R_g^2} = \frac{1}{n} \sum_{i \in C_n} r_i^2, \tag{3}$$

As with the geodesic properties, the radius of gyration is reported as a function of cluster size, n, with its value averaged over all instances of clusters of size n.

A more refined description of aggregate shape can be obtained using computational topology, specifically persistent homology (PH), which describes the 3-dimensional arrangement of point cloud data. Over the last decade there has been tremendous growth of applied mathematics methods that have combined the concepts of algebraic topology and computation with the aim of characterizing the global shape of data.[33,34] Broadly called topological data analysis, persistent homology is a technique that produces a compact summary of the global shape of sets of points in the form of a barcode and has been recently employed to study ion aggregation in aqueous electrolytes.[35,36] Given a collection of point cloud data (in this case the position of the CC nodes), persistent homology provides an objective way to quantify and compare global shapes of the data sets.[37]

We begin by constructing a sequence of growing simplicial complexes, where each simplicial complex is a collection of vertices, edges, triangles, and higher order simplices glued together "nicely".[38] To create the growing simplicial complexes, a ball of diameter d is centered at each CC node and the diameter systematically grown (Figure 2). As the diameter grow, balls centered at CC nodes that are close to each other will intersect before those centered at CC nodes that are farther apart. As d is increased, the intersection of a pair of balls is captured by adding the edge connecting the points. Triangles, tetrahedra, and higher order simplices are added to capture higher order intersections of balls. The small connected components merge into bigger connected components that form the triangles and other simplices, while holes appear and disappear. The intersections of these balls over the entire range of values of d capture all information about the global shape of the malonomide aggregates, initially at the local level, then the aggregates as a whole, then aggregate-aggregate interactions, until the entire space of the simulation box is filled. The number of connected components in the object or space is monitored by the β_0 number (which relates to the original homology of the space), while the β_1 counts the number of holes present. The changes

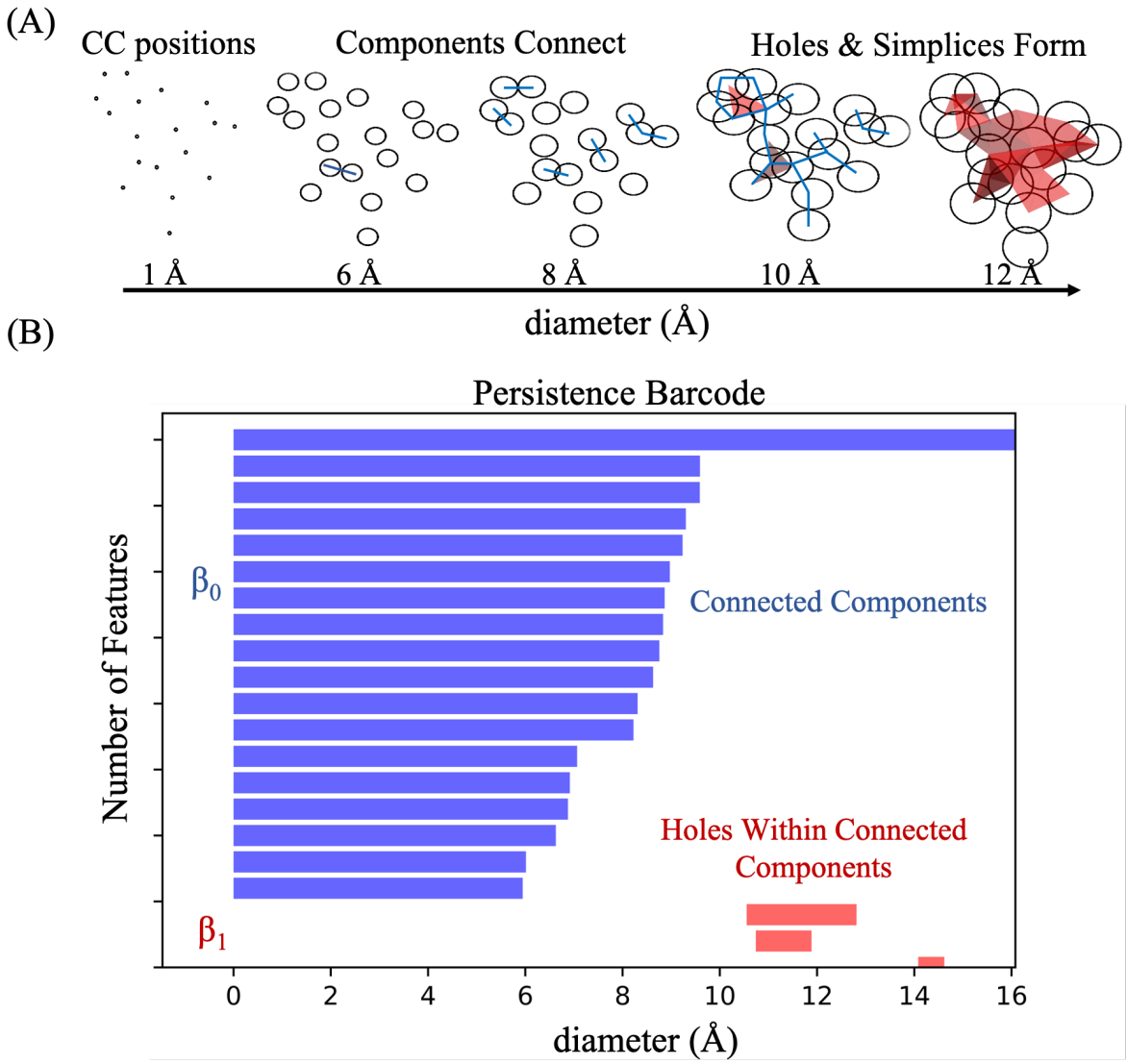

Figure 2: Construction of the persistent homology (PH) barcode from point cloud data based upon the CC positions of amphiphilic extractants. (A) Spheres centered on the CC positions have their diameter systematically increased, where individual spheres (components) merge to become connected and holes and voids form in 3-dimensional space and triangles and tetrahedra form simplicial complexes. (B) The number of connected components are counted (β_0) and the number of holes between amongst connected components are measured (β_1) as a function of sphere diameter to create the PH barcode.

to β_0 and β_1 values are tracked as d increases, and and this information is presented in a compact form as a barcode as illustrated in Figure 2. Persistence barcodes are obtained over a 50 ns trajectory at a sampling interval of 100 ps (1 barcode/frame of data). The persistent topological features are extracted by computing the persistent betti number, defined as the sum of all persistent k^{th} dimensional features within a specified interval of the ball diameter. The emergence (or birth) and disappearance (or death, caused by merging of features) of β_0 and β_1 along the d axis is tracked to identify the topologically relevant important lengthscales of spatial organization.

3 Results and Discussion

Malonamide self-association and solution structure is driven by a balance between dipole-dipole and steric interactions. By constraining malonamides to specific conformational isomers, we demonstrate a clear link between malonamide conformations that feature larger molecular dipoles and stronger self-association. Then, we investigate unconstrained malonamide solutions structures and demonstrate that, at higher concentrations, malonamide-malonamide steric contributions become relevant and influence both the patterns of intermolecular interactions as well as spatial distribution within and between aggregates.

3.1 Fixed Conformation Simulations

Characteristics of the Constrained Systems. Malonamide conformation is an essential aspect of its ability to coordiante metal ions[39–41] and has been correlated with changes in organic phase aggregation.[42] There are two primary degrees of freedom that define the conformation and modulate the molecular dipole: the relative orientation of the carbonyl C=O bond vectors[21,39–41,43] and the amide stereoisomerization.[42] As the former is a pseudo-dihedral, we define it as the angle between the C=O bond vectors. The latter is defined by the O−C−N−Me dihedral angle. The relative C=O orientation is classified as either *gauche*

(angles less than 120°) or *trans* (angles greater than 120°), as justified by the probability distribution of the angle between C=O vectors (Figure S1).[21,43] For the O−C−N−Me dihedral angle, each amide group is defined as Z or E,[42] as illustrated in Figure 1, with the O−C−N−Me angle cutoff between the E (methyl group in *gauche* position) and Z (methyl group in *trans* position) stereoisomers of 90°.

Table 2: The average molecular dipole values are given here for each combination of constrained relative C=0 vector orientation and conformational isomerization simulations.

	DMDOHEMA dipole (debye)			DMDBTDMA dipole (debye)		
	All *gauche*	All *trans*	Not constrained	All *gauche*	All *trans*	Not constrained
All E	6.75	2.90	—	7.28	2.05	—
All Z	—	3.04	—	—	2.15	—
2:1 Z:E	6.05	2.96	—	6.70	2.15	—
Not constrained	—	—	3.84	—	—	2.03

At a concentration of 0.5 M, five combinations of C=O orientation and amide conformational isomerization were considered: *gauche* C=O vectors with a) all E and, b) a 2:1 Z:E ratio, and *trans* C=O vectors with c) all Z, d) all E and e) a 2:1 Z:E ratio. The 2:1 ratio is the approximate distribution expected based on NMR spectroscopy.[42] Constraints were imposed by increasing the O−C−N−Me torsion barrier to 400 kJ/mol, which also fixed the C=O orientation (see Table S1 for the fraction of *trans* C=O vectors for each constrained system). Initial malonamide configurations were changed to match the fixed geometry of interest; for the 2:1 Z:E ratio, Z and E conformations were generated randomly assuming that conformational isomerization of amide groups within the same molecule are statistically independent.[42] The time evolution of the spatial distribution of the system, as analyzed by the persistent homology, is shown in Figure S2 to demonstrate adequate equilibration of the solution structure. The molecular dipole moments, calculated as the ensemble average values of the sum of the distances of every atom site from the malonamide center of mass and weighted by the atomic charge, are presented in Table 2 within each set of constrained sim-

ulations. The relative malonamide orientation is defined as the angle between two vectors: the bisector of the O-CC-O angle for each molecule, where the O atoms sites are the O-atoms of the two amide groups. The probability density function of the angle, $P(\theta)$, normalized by $\sin(\theta)$, are plotted in Figure S3 for all fixed internal geometry 0.5 M simulations. Notably, within constrained geometry simulations orientational preferences of the molecular dipoles are observed, when in the *gauche* C=O vector conformation DMDBTDMA strongly prefers parallel dipole alignment while DMDOHEMA does not.

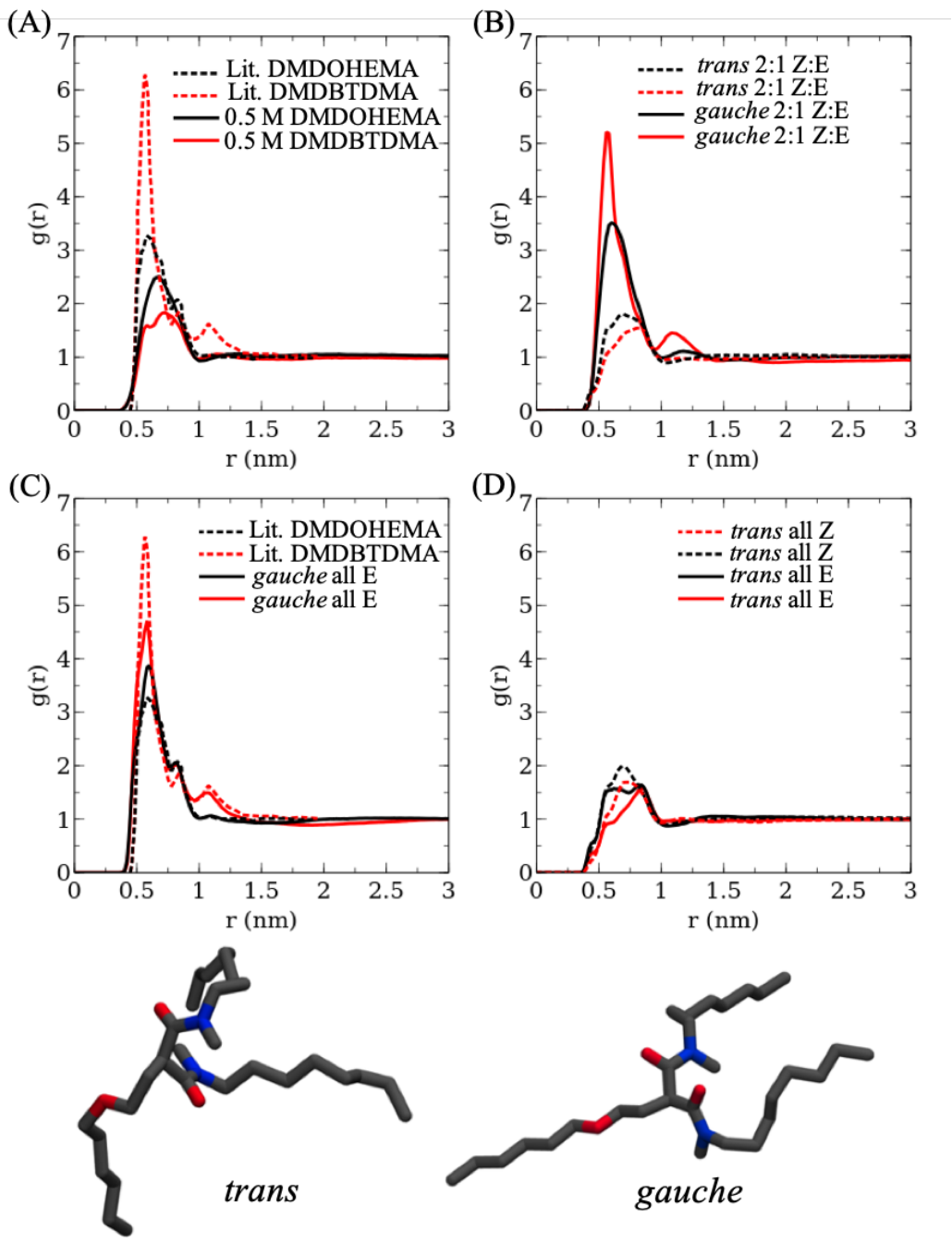

Figure 3: Comparison of RDFs for the 0.5 M solutions. (A) The unconstrained CC-CC RDFs from this study overlayed with those prior literature[19] (using the OPLS force field in n-heptane). (B) the CC-CC RDFs for the constrained geometries having fixed 2:1 Z:E ratios for both *trans* and *gauche* C=O vectors. (C) Comparison of the prior literature RDFs with the constrained *gauche* C=O vectors having all E conformational isomerization, (D) CC-CC RDFs at the constrained *trans* conformations with all E or all Z.

The relative malonamide orientations are correlated with the primary and secondary peaks of the CC-CC RDFs,[26] and their respective heights are used as an initial indication of self-association (Figure 3). Importantly, both descriptors of internal malonamide geometry impact self-association The *gauche* conformation of C=O vectors dramatically increase the height of the first correlation peak for both malonamides. In the absence of the strong first peak, the impact of the Z:E ratio on the peak heights of the weaker, secondary correlations at larger CC-CC distances is also apparent. Overall, these results substantiate the conclusion that the largest impact on molecular dipole—and self-association that derives from dipole interactions—originates from the relative C=O vector orientation.

Intermolecular Networks and Spatial Organization. These data are further examined using cluster analysis of the intermolecular interaction networks and persistent homology so as to understand the role of the molecular conformation upon the aggregate size distribution and spatial organization. A detailed comparison is presented for the *gauche* 2:1 Z:E simulation versus the unconstrained simulation data. As observed in Figures 4A - 4B, imposing the constraint clearly increases the average cluster size, with a more significant affect being observed for DMDBTDMA, consistent with the larger molecular dipole of DMDBTDMA and smaller alkyl chain lengths (presumably with reduced alkyl sterics). Figure S4 presents a log-scale plot up to the largest, rare, clusters observed with sizes in the several hundred. Graph analysis of the intermolecular interaction network within each cluster further reveal longer network pathways within those clusters in the constrained simulations (Figure S5). Such information can reflect changes to internal connectivity as well as associated spatial distributions. To delve deeper into this topic, the number of connected components β_0 as a function of distance was first examined (Figure 4C). For all systems, a rapid drop in β_0 is observed immediately preceding 0.5 nm that is commensurate with the growth of intermolecular interactions between CC nodes that cause components to merge and the formation of the intermolecular network used to define self-association and cluster-

ing. The merger of connected components rapidly continues from 0.5 nm to 1 nm, where the constrained systems have steeper slopes than the unconstrained analogues consistent with self-assembly. Interestingly, analysis of the β_1 holes reveals that cycles/holes of CC nodes do not form until $\sim$ 0.7 nm. The constrained simulations have a larger increase in β_1 holes as the diameter of the CC nodes intersect to form cycles at lower distance relative to the unconstrained simulations, which supports increased self-association defined by more densely packed molecular assemblies within the constrained simulations.

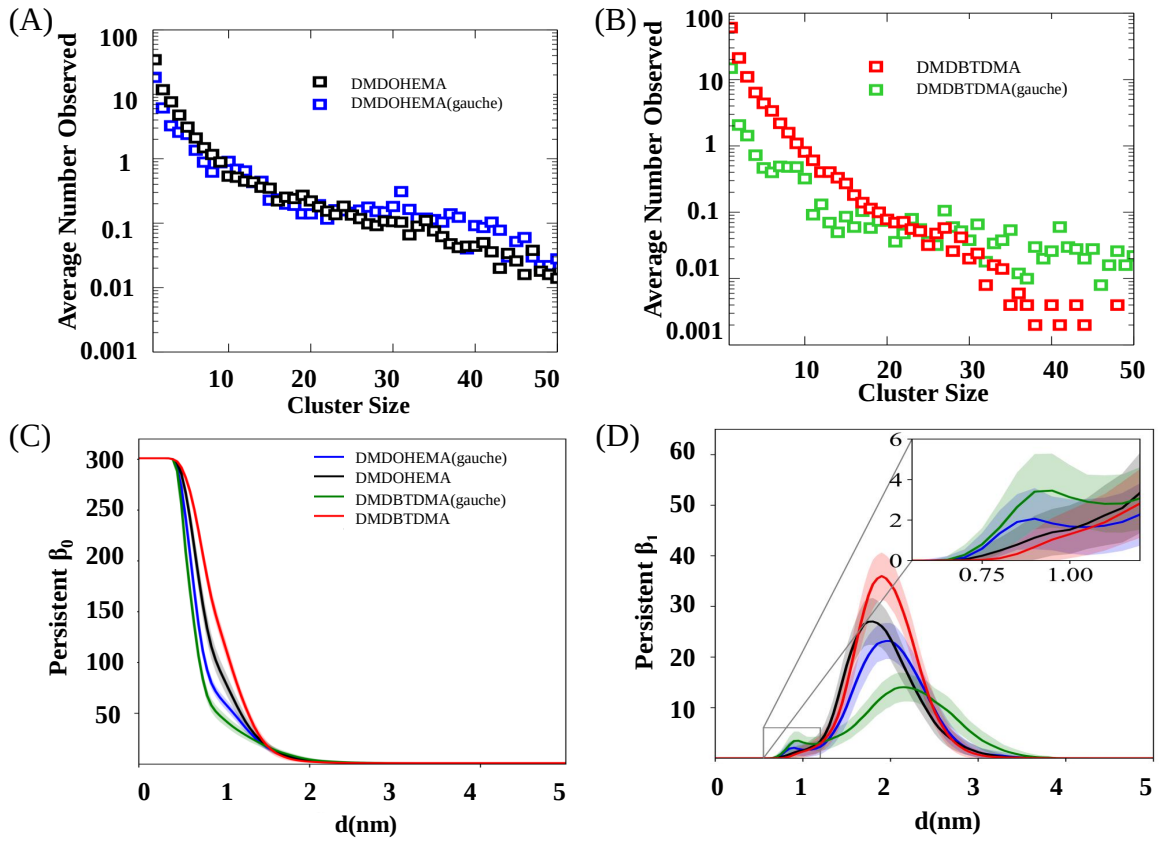

Figure 4: Comparison of cluster distributions and persistent homology betti numbers at 0.5 M DMDOHEMA or DMDBTDMA under constrained *gauche* 2:1 Z:E conformation and unconstrained conditions. (A) The cluster size distribution of DMDOHEMA. (B) The cluster size distribution of DMDBTDMA. (C) The variation of average persistent β_0 betti number (and β_1) with the increasing filtration value for 0.5 M DMDBTDMA and DMDOHEMA with and without the applied constraints. (D) The variation of average persistent β_1 betti number with the increasing filtration value for 0.5 M DMDBTDMA and DMDOHEMA with and without the applied constraints. Note that the error bar in the plot indicates the standard deviation of persistent betti numbers of all the frames within the window of 0.5 Å.

Interestingly, the steepness of the slope of the β_0 distribution exhibits a distinct change at approximately 1 nm that is most pronounced for the constrained simulations; this is complemented by a bimodal distribution in the β_1 values that is only observed within the constrained simulations. Together, these data indicate two characteristic length scales associated of organization when self-assembly is enhanced. The local spatial topology of CC nodes is somewhat different for the constrained variants of DMDOHEMA and DMDBTDMA, as indicated by the different shapes of the β_1 distribution (Figure 4D). Under 1 nm, the constrained DMDBTDMA forms a larger number of 1D holes (higher peak in the distribution) within the connected components relative to the constrained DMDOHEMA. Noticeably, the presence of a minimum after the peak at $\sim$ 1.2 nm indicates that the empty space between the molecular nodes gets rapidly filled with the growth of the diameter centered on the CC position. This indicates enhanced local intermolecular association of constrained DMDBTDMA when compared with constrained DMDOHEMA within a distance of 1 nm. Beyond a diameter of 1.2 nm, new growth of β_1 values indicates inter-aggregate hole formation caused by aggregate-aggregate interactions. Comparison of the constrained simulations indicates that variations in the local aggregation also impact longer-distance solution structure. The DMDOHEMA is less able to form longer-range inter-aggregate associations (less holes in the blue β_1 distribution at longer distance) relative to DMDBTDMA (the green β_1 distribution). Further, there is a relationship between the extent of local aggregation, local aggregate size, and longer-range solution structure. These are illustrated by comparing the blue and black curves in the β_1 distribution in Figure 4D, while for DMDTDMA the green vs. red curves are relevant. More clusters of larger size (in the case of DMDBTDMA) form extended spatial aggregate-aggregate interactions that are manifested in the formation of holes at longer distances (relative to DMDOHEMA).

3.2 Equilibrium Aggregation Behavior

Conformational Distributions. Equilibrium unconstrained simulations explore the malonamide conformational ensembles observed under realistic conditions and support an expanded view of how conformation is related to phase phenomena. Despite its importance, as demonstrated above, the impact of malonamide conformation has not been discussed in the malonamide simulation literature.[18–20,44–49] The goal of the current discussion is to link the equilibrium malonamide chemical structure to changes in self-association and then describe how those changes lead to differences in the cluster size distribution, the characteristics of the intermolecular interactions within an aggregate, and aggregate shape.

We begin by discussing the predicted and experimental solution structural features with consideration of the ensemble distribution of equilibrium conformations. The unconstrained malonamide conformation simulations allow the malonamide molecules to interconvert between relative C=O orientations and Z/E conformational isomers. The time evolution of the spatial distribution of molecules, demonstrating equilibration of resulting solution structure across scale is presented in Figure S6. Electronic structure calculations show that the gas phase electronic energy of the *trans* conformation is about 3 kcal/mol more favorable than the *gauche* conformation.[39–41] For condensed phase simulations with dipole-dipole self-associating malonamides, we expect the *gauche* conformation to be more favorable than in the gas phase.[39] As shown in Table 3, the fraction of malonamides in the *trans* conformation in the equilibrium simulations is consistent with this expectation. Similarly, the fraction of Z conformational isomers is consistent with the approximately 2:1 ratio from NMR for similar systems.[42]

In prior work we have described how organic phase structure—as observed in small angle scattering—stems from electron density heterogeneities introduced by dipole-dipole association, even in the absence of a reverse micellar structure as presumed in the literature.[26] The simulations in this work are consistent with the concentration dependent solution structure

Table 3: Thermophysical and conformational properties for each equilibrated system. The total density of each system is reported. For malonamides, their concentration, average molecular dipole, self-diffusion coefficient and configurational descriptors are given.

Malonamide type	Conc. [mol/L]	Dipole (debye)	Density (g/cm^3)	D ($\times 10^{-6} cm^2/s$)	Fraction Z	Fraction *trans*
DMDOHEMA	0.5	3.84	816.5	0.28	0.75	0.72
DMDOHEMA	1.1	3.57	861.0	0.10	0.76	0.81
DMDOHEMA	1.5	3.46	889.9	0.05	0.76	0.85
DMDBTDMA	0.5	2.03	810.9	0.39	0.80	0.99
DMDBTDMA	1.1	2.32	846.5	0.12	0.78	0.94
DMDBTDMA	1.5	2.79	870.2	0.06	0.79	0.85

measured with SAXS: experimental SAXS data are compared to the SAXS profiles computed from the simulation trajectories in Figure S7, with details on experimental methodology and simulation-calculated scattering profiles provided in Servis et al.[26]. Correlation peak positions and relative intensities are all well reproduced.

The CC-CC RDF has been reported from prior simulations of DMDOHEMA and DMDBTDMA (in n-heptane),[19] but the relative peak positions are substantially different from those reported here, as shown with that data plotted with data from this study in Figure 3. This differences in CC-CC RDFs between the unconstrained simulations in this work and the prior RDFs can be entirely explained by differences in conformation. Despite being modeled with the OPLS force field (versus GAFF used here), the prior simulation the malonamide were fixed in the *gauche* C=O vector configuration with all E conformational isomerization. Presumably, the larger O−C−N−Me torsion barrier in the OPLS force field implemented in the prior study[19] fixed the internal geometry of the malonamide molecules to the initial uniform conformation and did not allow for equilibration of the conformational isomers. This is consistent with visual inspection of snapshots provided by Qiao et al.[19]. Visual inspection of other reported MD simulations which do not provide diagnostic data, such as the CC-CC RDF or molecular dipole, also indicate the same conformation for all malonamide molecules.[18–20,44–49] Importantly, the restricted sampling of conformational isomers also impacts other characterization probes of solution structure, like SAXS. As observed in Figures

S8-S9, in comparison to experiment, the constrained simulation of the *gauche* all E conformational isomers have a demonstrable variation whereas the equilibrium simulations are in much better agreement.

This important observation points to the necessity of testing the energetic characteristics of intramolecular potentials of the relevant conformational degrees of freedom in structurally complex amphiphiles so as to ensure proper ergodic sampling. The fact that the malonamides in this study are able to interconvert over simulation-accessible length scales, and therefore sample more than the single initial configuration, lends confidence to the molecular model employed. Given that we demonstrate the strong sensitivity of self-association to malonamide conformation and the response of malonamide conformation to its local environment—as demonstrated by its concentration dependence—future simulation studies should treat malonamide conformation carefully to avoid generating configurational ensembles which simply reproduce the initial configuration.

Moving on to a more detailed study of the equilibrium distribution of conformations as a function of concentration (Table 3), we first consider the relative orientation of associating malonamides. The probability density function of the angle, $P(\theta)$, normalized by $\sin(\theta)$, are plotted in Figure 5 at each concentration. At 0.5 M, neither malonamide shows a strong orientational preference: the large fraction of *trans* C=O vectors for DMDBTDMA reduces the molecular dipole driver for strong orientational preference while DMDOHEMA sterics—discussed below—prevent their strong alignment. At higher concentration, where more *gauche* conformations are present for DMDBTDMA, a noticeable orientational preference emerges for *gauche* alignment, corresponding to values of θ near 0°. While it is intuitive that dipole alignment is weak for the low-dipole *trans* C=O conformation, this does not explain why only DMDBTDMA shows dipole alignment at high concentration—DMDOHEMA has a larger molecular dipole and the same fraction of *trans* C=O vectors at 1.5 M. The impact of the relative C=O orientation on molecular dipole is clear: the approximately *gauche* configuration, where the carbonyl dipoles are more aligned compared to the *trans*

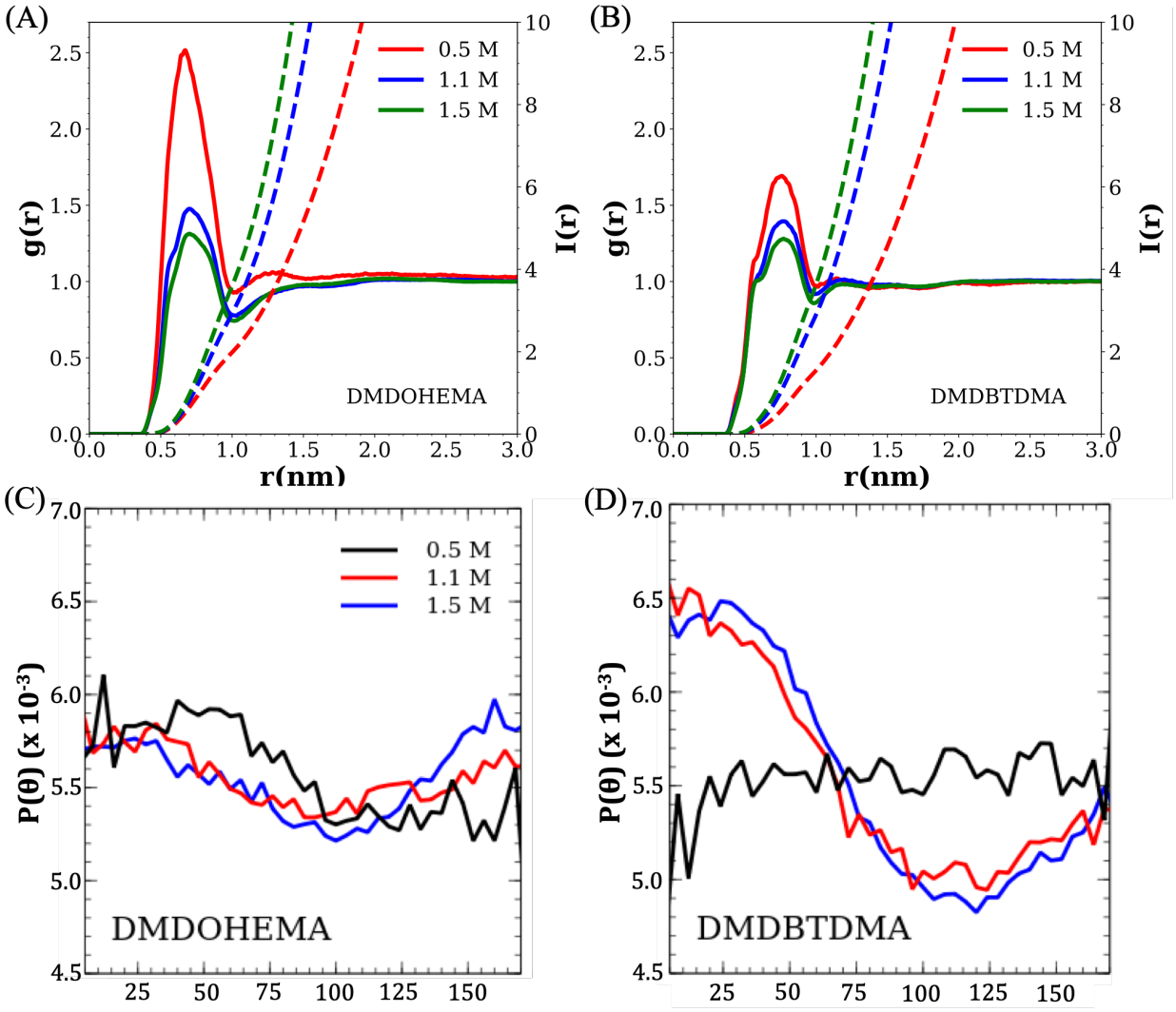

Figure 5: The CC-CC radial distribution functions are plotted for (A) DMDOHEMA and (B) DMDBTDMA for all systems. Line color corresponds to malonamide concentration. Probability distribution of the angle θ between molecular dipoles under constrained simulation conditions for (C) DMDOHEMA and (D) DMDBTDMA. The relative malonamide orientation is defined as the angle between two vectors: the bisector of the O-CC-O angle for each molecule, where the O atoms sites are the O-atoms of the two amide groups. The probability density function of the angle, P(θ), is normalized by sin(θ).

configuration, results in a larger average molecular dipole.

Relating this to the CC-CC RDFs, clearly points to a correlation of the aligned dipoles with increased malonamide self-association. At low concentration, DMDOHEMA shows higher self-association than DMDBTDMA, which is largely explained by the increased propensity of DMDOHEMA for the *gauche* configuration. The conformational isomerization has, as expected, a smaller impact on the molecular dipole. The fraction of amide groups in the Z conformation is largely constant between malonamides and the concentrations and are close to the experimentally determined value of approximately two thirds.[42] The difference in association, as indicated by the RDFs decreases with increasing concentration. This trend is explained by the difference in molecular dipole between the two molecules and between concentrations, as shown in Table 3. At low concentration, the difference in dipole between DMDOHEMA and DMDBTDMA is largest (3.84 vs. 2.03 debye, respectively), while at higher concentrations the difference is reduced.

Cluster Characteristics. Given the impact of chemical structure on the relative orientation of associating malonamides, the effect of that orientation on aggregate size, connectivity of intermolecular interactions, and shape is investigated. First, aggregates are quantified by clustering analysis. As we previously reported for different concentrations and malonamide types, and evidenced by the malonamide cluster size distributions in Figure 6, there is no characteristic size for aggregate formation at 0.5 M: the cluster sizes follow an approximately power law distribution. At higher concentrations, most malonamide molecules belong to a single system-spanning cluster.[26] As one might anticipate from studying the number of connected components β_0 within the persistent homology, increasing the concentration of the malonomides causes sharper decreases to β_0 as a function of the diameter, consistent with the formation of a system spanning cluster. At a diameter of 1 nm within the 0.5 M solutions, 28 % of all connected components remain for DMDOHEMA, whereas 40 % remain for DMDBTDMA. Yet at 1.5 M concentration only 2 - 3 % of all components remain for both

malonomides. More than 99 % of the original number of components have been merged into a single simplicial complex at 1.2 nm for both systems.

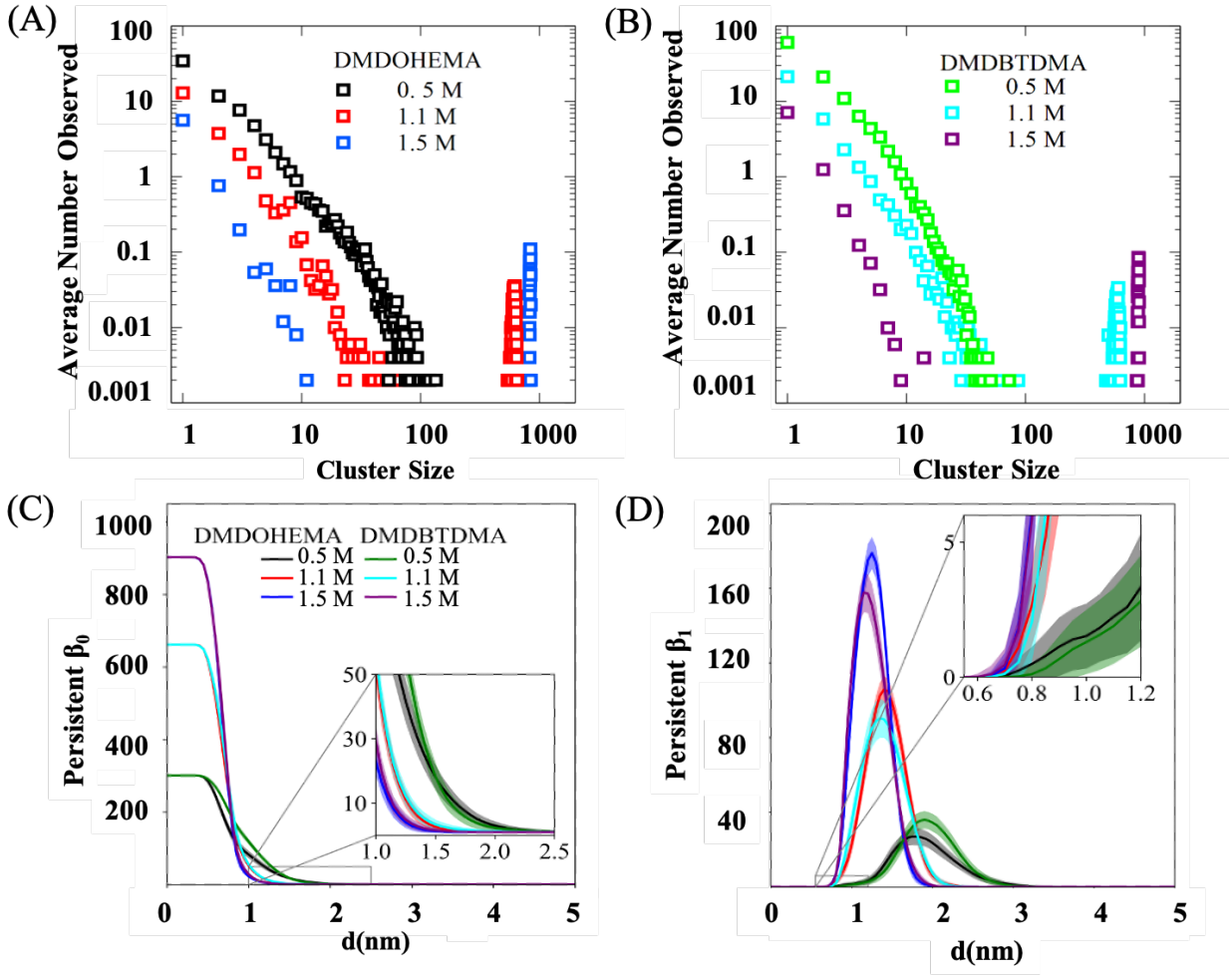

Figure 6: Comparison of cluster distributions and persistent homology betti numbers at 0.5, 1.1, and 1.5 M DMDOHEMA or DMDBTDMA. (A) The cluster size distributions of DMDOHEMA. (B) The cluster size distribution of DMDBTDMA. (C) The variation of average persistent β_0 betti number (and β_1) with the increasing filtration value as a function of concentration of DMDBTDMA and DMDOHEMA ligands. (D) The variation of average persistent β_1 betti number with the increasing filtration value as a function of concentration of DMDBTDMA and DMDOHEMA. Note that the error bar in the plot indicates the standard deviation of persistent betti numbers of all the frames within the window of 0.5 Å.

Relationships Between Intermolecular Interactions and Spatial Distribution. The organization within aggregates was quantified both in terms of the intermolecular interactions as well as spatial distribution. First, we quantify the topology of the intermolecular

network of interactions using the global clustering coefficient, which is averaged over all clusters of a given size, plotted in Figure 7. Snapshots in Figure S5 show example 5-mer clusters for DMDOHEMA and DMDBTDMA with global clustering coefficients of 1/3 and 1/5, respectively. First, we note that the clustering coefficient is largely consistent across the range of observed cluster sizes for each system. This is consistent with the observed lack of characteristic aggregate size: there is no fundamental, dramatic change in the topology of the intermolecular network of interactions across different discrete cluster sizes and, similarly, no fundamental difference in network structure between the discrete clusters and the dense, spanning clusters.

For each system, for all cluster sizes, the global clustering coefficient is lower for DMDBTDMA than DMDOHEMA. This indicates that the network of individual DMDOHEMA interactions more readily forms branch points within clusters, leading to more highly interconnected aggregates. The clustering coefficients, averaged from cluster sizes from 3 to 50 (monomers and dimers do not contain triplets) with error reported as the standard deviation between those cluster sizes, are 0.34 ± 0.02 for DMDOHEMA and 0.25 ± 0.03 for DMDBTDMA. The trends in clustering coefficients are independent of edge definition. Choosing a 0.77 nm CC-CC cutoff distance for malonamide connectivity (corresponding only to the shoulder rather than the entire nearest neighbor peak) yields the same trend in clustering coefficient, with average values of 0.13 ± 0.015 for DMDOHEMA and 0.091 ± 0.027 for DMDBTDMA. These values are averaged are over 3- to 15-mers, given the lower overall clustering with the smaller cutoff, and the magnitude of the values are similarly reduced due to the reduction in the total number of edges. This trend is observed for the constrained *gauche* simulations as well, with 0.41 ± 0.03 and 0.35 ± 0.05 for the constrained *gauche* DMDOHEMA and DMDBTDMA, respectively. Therefore, the clustering coefficient is sensitive to the different tail structures of the two malonamides regardless of conformation. It should also be noted that the clustering coefficient is not simply the result of linear orientation, but is naturally increased by more overall association: the constrained *gauche* simulations, hav-

ing overall higher molecular dipoles and more malonamide self-association, as seen in Figure 3, show larger clustering coefficients. Therefore, the differences in clustering coefficient from tail structure should not be conflated with the differences from overall increased associated from conformation. Indeed, the difference between unconstrained and constrained *gauche* DMDBTDMA is roughly the same as the difference between unconstrained DMDBTDMA and unconstrained DMDOHEMA. This highlights the sensitivity, and therefore utility, of the clustering coefficient to distinguish both conformational and alkyl tail structural differences.

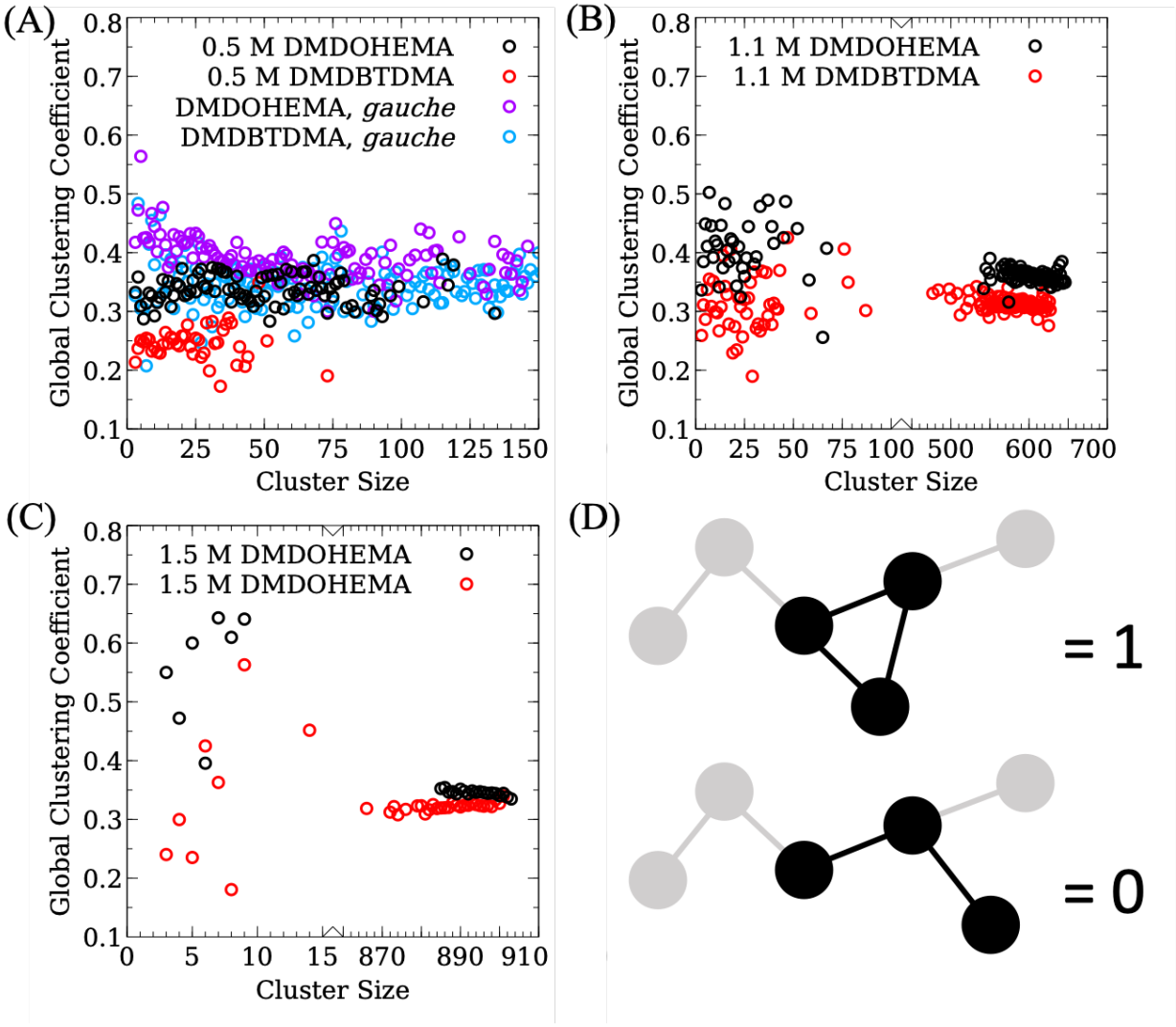

Figure 7: The global clustering coefficient is plotted as a function of cluster size for both malonamides for each concentration: (A) 0.5 M, (B) 1.1 M and (C) 1.5 M. (D) Illustration of two triplets within 6-mer clusters shows the contribution of those triplets to the global clustering coefficient.

Complementary to the clustering coefficient is the geodesic length of the intermolecular interactions within an aggregate, which contains information about how extended the structure is of the aggregate networks. This feature is quantified by the maximum shortest path (or maximum geodesic). The maximum geodesic is averaged over all clusters of a given size, and plotted in Figure 8 as a function of cluster size. The maximum shortest path lengths for the constrained *gauche* simulations are plotted in Figure S10. Due to the relatively small total path length differences between malonamides, the difference between path length values is plotted for the 0.5 M simulations. For the 0.5 M simulations, DMDBTMDA show, on average, larger maximum path lengths compared to DMDOHEMA.

The relationship between intermolecular network topology and spatial distribution is not always straightforward. As a metric of overall size of aggregates, the difference in cluster radius of gyration, R_g, is plotted in Figure S11 to quantify the difference in real space compactness of DMDBTDMA versus DMDOHEMA aggregates. The maximum geodesic and R_g difference between DMDOHEMA and DMDBTDMA track closely over the range of cluster sizes, which indicates that in this system the differences between malonamides in geodesic distance are reflective of analogous differences in the overall spatial extent of an aggregate: longer topological path lengths correspond to larger distances in real space. At high malonamide concentration, where a system-spanning cluster dominates, the maximum path length of that spanning cluster—while dependent on system size and malonamide concentration, both of which are fixed here—is smaller for DMDOHEMA than DMDBTDMA. Therefore, the dipole and steric influences that create the more linear DMDBTDMA clusters are lower concentration also determine the structure of the densely packed malonamide network at high concentration. Complementing this perspective, the β_1 distribution reflects the spatial distribution and presence of holes or voids amongst groups of components across lengthscale (Figure 4). At 0.5 M, the β_1 number distribution retains some of the bimodal characteristics apparent within the constrained simulations, where the higher average dipole moment of DMDOHEMA (3.84 D) than DMDBTDMA (2.03 D) correlates with the growth of β_1 holes

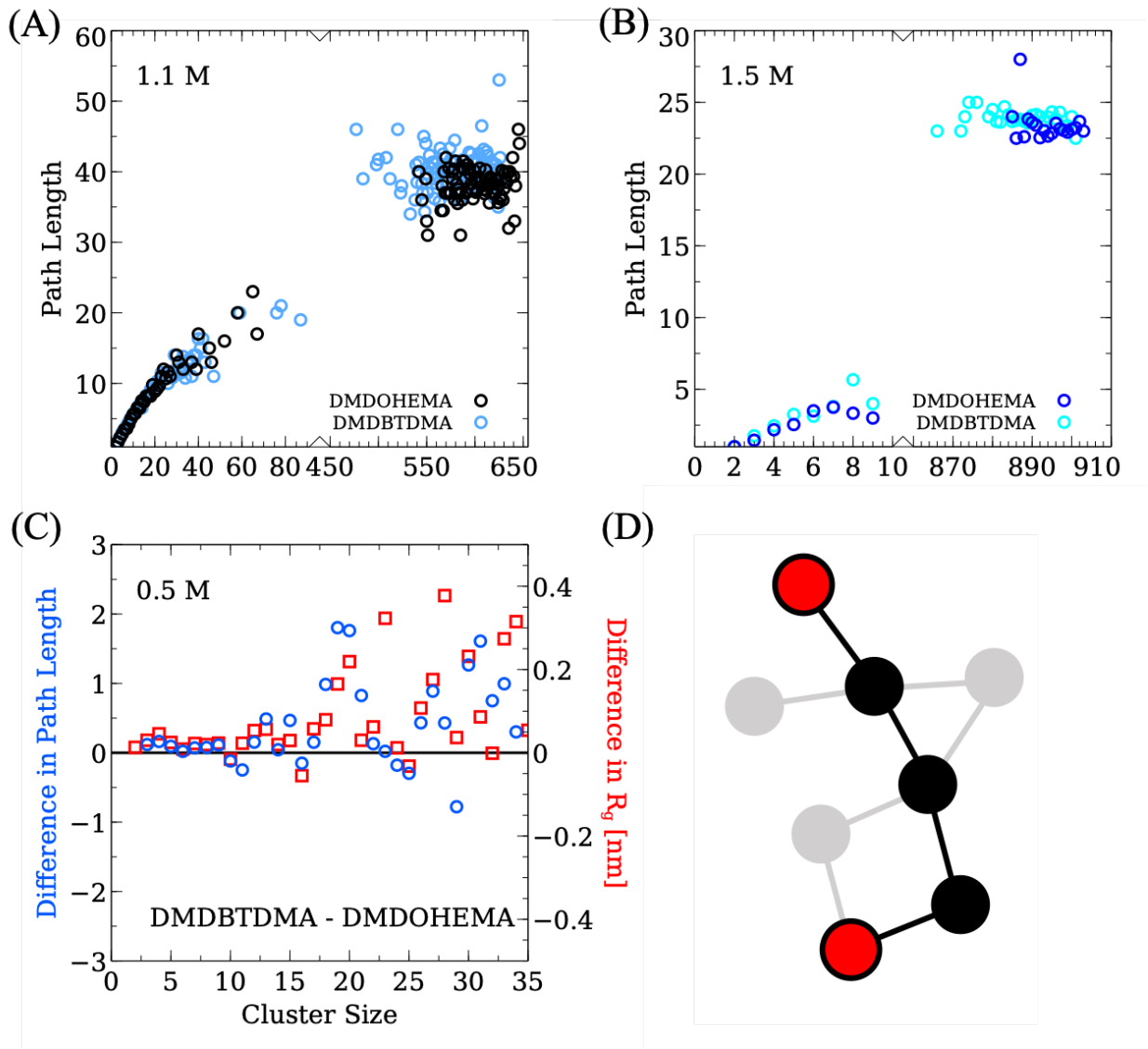

Figure 8: The average value of the maximum shortest path is plotted as a function of cluster size for (A) 1.1 and (B) 1.5 M malonamide simulations. (C) The difference between maximum shortest path lengths for the 0.5 M DMDBTDMA and DMDOHEMA systems is plotted (blue circles, left axis) along with the difference in cluster radius of gyration, R_g (red squares, right axis). (D) One of the possible maximum shortest paths (between red nodes, connected by black lines and black nodes) for an example cluster.

at smaller distances. However as the concentration is increased the distribution becomes unimodal. Concomitant to the smaller differences of dipole moments between the ligands at higher concentration, the growth of β_1 holes becomes more and more similar for both the ligands. Further, with higher concentration β_1 distribution peak gets shifted to smaller distance as a results of the dense packing of molecules that partially overcomes the steric factors observed at 0.5 M (where holes form at larger distances). Another distinct feature of these β_1 distributions is the associated peak height: at higher concentration DMDOHEMA has larger peak height when compared with DMDBTDMA, suggesting generation of more number of 1D holes for the former. This essentially reflects more organized circular ordering or "swiss cheese" structures in case of DMDOHEMA, and therefore nicely corroborates with the finding of geodesic analysis that suggested a more linearly connected DMDBTDMA aggregates as compared to DMDOHEMA.

4 Conclusions

Amphiphile self-association in non-polar media is of significant importance to a number of applications, not the least of which is liquid-liquid extraction. A significant opportunity exists to understand how molecular-scale conformation and architecture influences not only aggregate size distributions, but also morphology across scale–from local aggregation to the aggregate-aggregate interactions that occur at high concentrations. Using representative DMDOHEMA and DMDBTDMA malonomide extractants (commonly applied to f-element separations), this work clearly demonstrates that self-association and multiscale solution organization are driven by a balance between dipole alignment and alkyl tail sterics. Those forces are significantly impacted by malonamide conformation and alkyl tail molecular structure. This is the first simulation study to compare and contrast the impact of malonamide conformation and, to the best of our knowledge, the first to use potentials which do not incidentally constrain malonamides to their initial conformation.

The self-association driven by strong dipole alignment informs the resulting aggregation topology, as evidenced from detailed graph theoretical and persistent homology analyses. The lower clustering coefficients and larger geodesic path lengths for DMDBTDMA aggregates relative to DMDOHEMA show that DMDBTDMA forms more linear, less highly interconnected clusters than DMDOHEMA; this in turn influences longer range solution structure as measured by the β_0 and β_1 distributions from persistent homology. While the linearity of DMDBTDMA aggregation compared to DMDOHEMA has been inferred from small angle scattering in the literature,[19] this graph theoretic and persistent homology approach provides a molecular basis for the emergent self-assembly organization. Importantly, the linearity of DMDBTDMA aggregates relative to DMDOHEMA is solely due to self-association in the absence of any extracted aqueous solutes or micellization. Therefore, this property is inherent to the malonamide/alkane mixture and not necessarily a reflection of micelle morphology. Having explained the underlying dipole alignment and steric balance that underpins the morphology of malonamide aggregates and aggregate-aggregate interactions, we have provided a direct link between the conformation and molecular structure of the malonamide to its resulting solution mesostructure.

5 Acknowledgments

This work was supported by the U.S. Department of Energy (DOE), Basic Energy Sciences, Chemical Sciences, Geosciences, and Biosciences Division under contract DEAC02-06CH11357. This research used resources from the Center for Institutional Research Computing at Washington State University.

References

(1) Zhang, X.; Wang, C. Supramolecular amphiphiles. *Chemical Society Reviews* **2011**, *40*, 94–101.

(2) Yamada, Y. M.; Sarkar, S. M.; Uozumi, Y. Amphiphilic self-assembled polymeric copper catalyst to parts per million levels: click chemistry. *Journal of the American Chemical Society* **2012**, *134*, 9285–9290.

(3) Kabanov, A. V.; Kabanov, V. A. Interpolyelectrolyte and block ionomer complexes for gene delivery: physico-chemical aspects. *Advanced Drug Delivery Reviews* **1998**, *30*, 49–60.

(4) Shimizu, T.; Masuda, M.; Minamikawa, H. Supramolecular nanotube architectures based on amphiphilic molecules. *Chemical Reviews* **2005**, *105*, 1401–1444.

(5) Wang, Y.; Xu, H.; Zhang, X. Tuning the amphiphilicity of building blocks: controlled self-assembly and disassembly for functional supramolecular materials. *Advanced Materials* **2009**, *21*, 2849–2864.

(6) Molla, M. R.; Ghosh, S. Aqueous self-assembly of chromophore-conjugated amphiphiles. *Physical Chemistry Chemical Physics* **2014**, *16*, 26672–26683.

(7) Rydberg, J.; Cox, M.; Musikas, C.; Choppin, G. *Solvent Extraction Principles and Practices*, 2nd ed.; Marcel Dekker: New York, 2004.

(8) Bourgeois, D.; El Maangar, A.; Dourdain, S. Importance of weak interactions in the formulation of organic phases for efficient L/L extraction of metals. *Current Opinion in Colloid & Interface Science* **2020**,

(9) Dozol, H.; Berthon, C. Characterisation of the supramolecular structure of malonamides by application of pulsed field gradients in NMR spectroscopy. *Physical Chemistry Chemical Physics* **2007**, *9*, 5162–5170.

(10) Meridiano, Y.; Berthon, L.; Crozes, X.; Sorel, C.; Dannus, P.; Antonio, M. R.; Chiarizia, R.; Zemb, T. Aggregation in Organic Solutions of Malonamides: Consequences for Water Extraction. *Solvent Extraction and Ion Exchange* **2009**, *27*, 607–637.

(11) Erlinger, C.; Gazeau, D.; Zemb, T.; Madic, C.; Lefrancois, L.; Hebrant, M.; Tondre, C. Effect of nitric acid extraction on phase behavior, microstructure and interactions between primary aggregates in the system dimethyldibutyltetradecylmalonamide (DMDBTDMA)/n-dodecane/water: A phase analysis and small angle X-ray scattering (SAXS) characterisation study. *Solvent Extraction and Ion Exchange* **1998**, *16*, 707–738.

(12) Erlinger, C.; Belloni, L.; Zemb, T.; Madic, C. Attractive interactions between reverse aggregates and phase separation in concentrated malonamide extractant solutions. *Langmuir* **1999**, *15*, 2290–2300.

(13) Dozol, H.; Berthon, C. Characterisation of the supramolecular structure of malonamides by application of pulsed field gradients in NMR spectroscopy. *Phys. Chem. Chem. Phys.* **2007**, *9*, 5162–5170.

(14) Bauduin, P.; Testard, F.; Berthon, L.; Zemb, T. Relation between the hydrophile/hydrophobe ratio of malonamide extractants and the stability of the organic phase: Investigation at high extractant concentrations. *Physical Chemistry Chemical Physics* **2007**, *9*, 3776–3785.

(15) Abécassis, B.; Testard, F.; Zemb, T.; Berthon, L.; Madic, C. Effect of n-octanol on the structure at the supramolecular scale of concentrated dimethyldioctylhexylethoxymalonamide extractant solutions. *Langmuir* **2003**, *19*, 6638–6644.

(16) Ellis, R. J.; D'Amico, L.; Chiarizia, R.; Antonio, M. R. Solvent Extraction of Cerium(III) Using an Aliphatic Malonamide: The Role of Acid in Organic Phase Behaviors. *Separation Science and Technology* **2012**, *47*, 2007–2014.

(17) Ellis, R. Critical Exponents for Solvent Extraction Resolved Using SAXS. *Journal of Physical Chemistry B* **2014**, *118*, 315–322.

(18) Ferru, G.; Rodrigues, D.; Berthon, L.; Diat, O.; Bauduin, P.; Guilbaud, P. Elucidation of the Structure of Organic Solutions in Solvent Extraction by Combining Molecular Dynamics and X-ray Scattering. *Angewandte Chemie* **2014**, *53*, 5346–5350.

(19) Qiao, B.; Littrell, K. C.; Ellis, R. J. Liquid worm-like and proto-micelles: water solubilization in amphiphileoil solutions. *Physical Chemistry Chemical Physics* **2018**, *20*, 12908–12915.

(20) Guilbaud, P.; Zemb, T. Depletion of water-in-oil aggregates from poor solvents: Transition from weak aggregates towards reverse micelles. *Current Opinion in Colloid & Interface Science* **2015**, *20*, 71–77.

(21) Servis, M. J.; Piechowicz, M.; Soderholm, L. Impact of Water Extraction on Malonamide Aggregation: A Molecular Dynamics and Graph Theoretic Approach. *The Journal of Physical Chemistry B* **2021**, *125*, 6629–6638.

(22) Baldwin, A.; Servis, M.; Yang, Y.; Bridges, N.; Wu, D.; Shafer, J. The Structure of Tributyl Phosphate Solutions: Nitric Acid, Uranium (VI), and Zirconium (IV). *Journal of Molecular Liquids* **2017**, *246*, 225–235.

(23) Nash, K.; Braley, J. *Advanced Separation Techniques for Nuclear Fuel Reprocessing Waste Treatment*; Woodhead Publishing Series in Energy: Cambridge, UK, 2011; Chapter Chemistry of Radioactive Materials in the Nuclear Fuel Cycle, pp 3–22.

(24) Abraham, M.; Murtol, T.; Schulz, R.; Pall, S.; Smith, J.; Hess, B.; Lindhal, E. GROMACS: High performance molecular simulations through multi-level parallelism from laptops to supercomputers. *SoftwareX* **2015**, *1-2*, 19–25.

(25) Wang, J.; Wolf, R.; Caldwell, J.; Kollman, P.; Case, D. Development and testing of a general amber force field. *Journal of Computational Chemistry* **2004**, *25*, 1157–1174.

(26) Servis, M. J.; Piechowicz, M.; Shkrob, I. A.; Soderholm, L.; Clark, A. E. Amphiphile Organization in Organic Solutions: An Alternative Explanation for Small-Angle X-ray Scattering Features in Malonamide/Alkane Mixtures. *The Journal of Physical Chemistry B* **2020**, *124*, 10822–10831, PMID: 33200612.

(27) Hockney, R. W.; Goel, S. P.; Eastwood, J. Quiet High Resolution Computer Models of a Plasma. *Journal of Computational Physics* **1974**, 148–158.

(28) Hess, B.; Bekker, H.; Berendsen, H.; Fraaije, J. LINCS: A constrained solver for molecular simulations. *Journal of Computational Chemistry* **1997**, *18*, 1463–1472.

(29) Darden, T.; York, D.; Pedersen, L. An N·log(N) method for Ewald sums in large systems. *Journal of Chemical Physics* **1993**, 10089–10092.

(30) Berendsen, H.; Postma, J.; van Gunsteren, W.; DiNola, A.; Haak, J. Molecular dynamics with coupling to an external bath. *Journal of Chemical Physics* **1984**, *81*, 3684.

(31) Hoover, W. Canonical dynamics: Equilibrium phase-space distributions. *Physical Review A* **1985**, *31*, 1695–1697.

(32) Wilson, R. J. *Introduction to Graph Theory*; Oliver and Boyd, Edinburgh, 1972.

(33) Carlsson, G. Topology and data. *Bulletin of the American Mathematical Society* **2009**, *46*, 255–308.

(34) Edelsbrunner, H.; Harer, J. L. *Computational Topology An Introduction*; American Mathematical Society, 2009.

(35) Ghrist, R. Barcodes: The persistent topology of data. *Bulletin of the American Mathematical Society* **2008**, *45*, 61–75.

(36) Xia, K. Persistent homology analysis of ion aggregations and hydrogen-bonding networks. *Physical Chemistry Chemical Physics* **2018**, *20*, 13448–13460.

(37) Edelsbrunner, H.; Letscher, D.; Zomorodian, A. Topological persistence and simplification. *Discrete and Computational Geometry* **2002**, *28*, 511–533.

(38) Munkres, J. R. *Elements of Algebraic Topology*; Addison–Wesley Publishing Company: Menlo Park, 1984; pp ix+454.

(39) Diss, R.; Wipff, G. Lanthanide cation extraction by malonamide ligands: from liquid–liquid interfaces to microemulsions. A molecular dynamics study. *Physical Chemistry Chemical Physics* **2005**, *7*, 264–272.

(40) Sandrone, G.; Dixon, D. A.; Hay, B. P. Conformational Analysis of Malonamide, N, N -Dimethylmalonamide, and N, N, N , N -Tetramethylmalonamide. *The Journal of Physical Chemistry A* **1999**, *103*, 3554–3561.

(41) Lumetta, G. J.; Rapko, B. M.; Garza, P. A.; Hay, B. P.; Gilbertson, R. D.; Weakley, T. J.; Hutchison, J. E. Deliberate design of ligand architecture yields dramatic enhancement of metal ion affinity. *Journal of the American Chemical Society* **2002**, *124*, 5644–5645.

(42) Lefrançois, L.; Delpuech, J. J.; Hébrant, M.; Chrisment, J.; Tondre, C. Aggregation and protonation phenomena in third phase formation: An NMR study of the quaternary malonamide/dodecane/nitric acid/water system. *Journal of Physical Chemistry B* **2001**, *105*, 2551–2564.

(43) Servis, M. J.; Piechowicz, M.; Skanthakumar, S.; Soderholm, L. Molecular-scale origins of solution nanostructure and excess thermodynamic properties in a water/amphiphile mixture. *Physical Chemistry Chemical Physics* **2021**, *23*, 8880–8890.

(44) Qiao, B.; Demars, T.; Olvera de la Cruz, M.; Ellis, R. J. How hydrogen bonds affect the growth of reverse micelles around coordinating metal ions. *The Journal of Physical Chemistry Letters* **2014**, *5*, 1440–1444.

(45) Ellis, R.; Meridiano, Y.; Muller, J.; Berthon, L.; Guilbaud, P.; Zorz, N.; Antonio, M.; Demars, T.; Zemb, T. Complexation-Induced Supramolecular Assembly Drives Metal-Ion Extraction. *Chemistry: A European Journal* **2014**, *20*, 12796–12807.

(46) Chen, Y.; Duvail, M.; Guilbaud, P.; Dufrêche, J.-F. Stability of reverse micelles in rare-earth separation: a chemical model based on a molecular approach. *Physical Chemistry Chemical Physics* **2017**, *19*, 7094–7100.

(47) Duvail, M.; van Damme, S.; Guilbaud, P.; Chen, Y.; Zemb, T.; Dufrêche, J. The role of curvature effects in liquid-liquid extraction: assessing organic phase mesoscopic properties from MD simulations. *Soft Matter* **2017**, *13*, 5518–5526.

(48) Qiao, B.; Ferru, G.; Ellis, R. J. Complexation Enhancement Drives Water-to-Oil Ion Transport: A Simulation Study. *Chemistry–A European Journal* **2017**, *23*, 427–436.

(49) Duvail, M.; Dumas, T.; Paquet, A.; Coste, A.; Berthon, L.; Guilbaud, P. UO_2^{2+} structure in solvent extraction phases resolved at molecular and supramolecular scales: a combined molecular dynamics, EXAFS and SWAXS approach. *Physical Chemistry Chemical Physics* **2019**, *21*, 7894–7906.